www.sciencetranslationalmedicine.org/cgi/content/full/6/266/266ra173/DC1

Supplementary Materials for

White matter changes linked to visual recovery after nerve decompression

David A. Paul, Elon Gaffin-Cahn, Eric B. Hintz, Giscard J. Adeclat, Tong Zhu, Zoë R. Williams, G. Edward Vates, Bradford Z. Mahon*

*Corresponding author. E-mail: mahon@rcbi.rochester.edu

Published 10 December 2014, *Sci. Transl. Med.* **6**, 266ra173 (2014)
DOI: 10.1126/scitranslmed.3010798

The PDF file includes:

Supplemental Methods

Additional details on participants

Patients were separated into two groups: compressive pituitary tumors (n = 9) with physical obstruction of the anterior visual pathway, and non-compressive pituitary tumors (n = 5) with no deformation of the optic nerve, chiasm, or tract (as determined by high resolution clinical MRI with contrast). Non-compressive pituitary tumor patients were managed either surgically or pharmacologically and underwent testing at only one time point before surgical intervention. Pre-operative DTI/fMRI data for a single compressive pituitary tumor patient were not acquired due to the presence of a coronary stent. A second compressive pituitary tumor patient was lost to follow-up after surgery and pre-operative visual fields could not be acquired in one patient. Seven of nine compressive pituitary tumor participants (14 optic tracts) successfully completed visual field performance testing (of whom six individuals had both pre- and post-operative DTI and visual fields data), and four of nine participants completed contrast sensitivity testing at both the pre- and post-operative time points (8 optic tracts). Lastly, DTI data for a single healthy control participant were not acquired due to claustrophobia.

A standard endoscopic endo-nasal approach was employed by the senior neurosurgeon, GEV, to achieve a gross total or near gross total resection of each pituitary tumor, leaving behind a normal pituitary gland and optic nerves (9). Refer to figure 1B in the main text for pre-and post-operative images of a representative sample of compressive pituitary tumor patients, demonstrating complete resection and decompression of the optic chiasm. It is important to note that this minimally invasive procedure does not violate the cerebrospinal fluid, and thus does not introduce potential artifacts for MRI, as would a craniotomy.

Additional Information on Visual Psychophysics

Visual Fields. On each trial, a single letter was presented to one of 90 locations across the visual field (organized into 15 bins of polar angle by six levels of eccentricity. Stimuli were fifteen black capital letters (A, C, F, H, K, L, N, P, Q, R, T, V, X, Y, Z) in Helvetica typeface. With the exception of ‘X,’ letter identity was a subset of letters used by Anstis 1974 (40). All letters were scaled to ten times the size of the discrimination threshold for each eccentricity (40). This ensured that identification errors were due to field defects rather than visual acuity limitations. Stimulus creation and display was controlled with the Psychophysics toolbox in

MATLAB (49, 50). Data from the visual field mapping experiments were analyzed by hemi-field (Figure 2C) and averaged within each participant group (compressive pituitary tumor patients, non-compressive pituitary tumor patients, and healthy control participants). For each hemi-field of each eye, visual field performance was defined as the percentage of correct responses. A weighted average of those values (e.g. 53% left eye temporal hemi-field and 47% right eye nasal hemi-field; see Supp. Figure S1) was used to summarize the visual field performance associated with each optic tract (51).

Contrast Sensitivity. Contrast sensitivity (CS) thresholds at each spatial frequency were obtained using a Bayesian algorithm that allows fast estimation of the CS curve (21). Each participant for whom we were able to collect data on contrast sensitivity completed 400 trials (100 trials per monocular hemi-field). For all analyses, contrast sensitivity was defined as the area under the log contrast sensitivity function (AULCSF) (21). As shown in Supp. Fig S2, AULCSF converges at 25 trials, and subsequent testing was performed to increase the precision of the measurement. As for visual fields, a weighted average of AULCSF for each hemi-field (53% for nasal fibers and 47% for temporal fibers) was used to analyze the contrast sensitivity function associated with each optic tract (51).

Detailed methods for tractography of the optic tract.

For each subject, the optic tract was first identified manually in the corresponding high-resolution T1-weighted image, which was then transformed into diffusion space. The seed was selected approximately 2-6 mm posterior to the optic chiasm in diffusion space, and identified as the voxel with the highest FA value. By restricting seed selection to voxels located posterior to the chiasm, we were able to consistently identify voxels with an anterior-posterior (green) principal eigenvector, as visualized with a color map in FSL (Supp. Figure S3A). Termination masks were placed in the LGN, chiasm and cerebral peduncles to regulate fiber tracking and avoid crossing fibers from the corticospinal tract (Supp. Figure S3B). 25,000 streamlines were sampled from the seed voxel and the final probability distribution for each fiber tract was thresholded at 2% (500) of the total number of streamlines. The threshold was determined through visual inspection of tractography results as the optimal value, which both removed outlying data points and preserved well-delineated optic tracts.

Analysis of variability in anterior-most point of optic tract across patients

Because it was necessary to manually define a seed voxel for probabilistic tractography of the optic tracts on a subject-by-subject basis, it was important to ensure that variability in the seed location was not coincidentally related to any of the diffusivity measures subsequently calculated. To reduce such variability, a single author, D.A.P, systematically placed all seeds. We also ruled out any relation between seed location and our observed effects in two ways. First, a one-way ANOVA that compared the y-dimension coordinate (in MNI space) of the anterior-most aspect of the optic tract from all participants (compressive pituitary tumor patients before and after surgery, non-compressive patient controls and healthy controls) indicated no differences across groups ($F_{(7,53)} = .8$, $p = .58$). This means that the anterior-most aspect of the optic tract across participant groups does not explain the observed group dissociations in diffusivity indices (e.g, Figures 3 and 4 in the main text). Second, we computed the correlation, for each segment of the optic tract, between the y-dimension coordinate of the anterior-most aspect of the tract and all four diffusivity measures (fractional anisotropy, mean diffusivity, axial diffusivity, and radial diffusivity). The resulting r-values, averaged across all segments of the optic tracts, indicated no correlation, for any index (mean r ± standard deviation: fractional anisotropy: r = -0.10 ±0.16; mean diffusivity: r = 0.01 ±0.16; axial diffusivity: r = -0.03±0.15; radial diffusivity: r = 0.03±0.17, all ts from one-sample t-tests < 1). This means that any variability in the "tractability" of the optic tracts through areas of significant tumor compression (as a result of the initial seed location) across participants was not related to any of the diffusivity measures obtained from the optic tracts.

Detailed Methods for Segmentation of the Optic Tracts

Both the right and left optic tracts from each subject were segmented into thirteen equidistant cross-sectional bins from the chiasm to the LGN using custom MATLAB scripts and implemented in two stages (see below). Diffusion indices (fractional anisotropy, mean diffusivity, axial diffusivity, and radial diffusivity) were then measured within each cross-sectional bin, and subsequently correlated with psychophysical data.

Along Tract Statistics Algorithm (Stage 1): During the first stage of our analysis, a mean-tract skeleton of the optic tracts (right and left) for each subject was generated in standard anatomical reference space using the MNI152 template brain. This stage (see steps 1-3 in Supp. Fig. 4), is similar to defining the thawleg (i.e. centerline) of a bathymetric river surface (46). To create the tract skeleton, the optic tracts of each individual

were normalized to the MNI152 reference template with the help of tract based spatial statistics in FSL. In order to avoid reorientation of diffusion tensors with image registration, the diffusion indices were calculated for all optic tract voxels in every subject's native diffusion space and then re-applied to the transformed voxels in MNI152 space. Thus, the final product of this registration step consisted of a normalized right and left optic tract for each subject, with preserved data points (i.e. fractional anisotropy, mean diffusivity, axial diffusivity and radial diffusivity) from the original native diffusion space within each normalized voxel.

Voxels from tract-normalized distributions of each study participant were then plotted in 3D and characterized by arc-angle with respect to a common reference point (44). In our case, MNI coordinates x=0, y=-25, which are centrally located with respect to the right and left optic tracts. Data were clustered into arc-angle segments with the maximum number of bins optimized so that every segment contained at east one data point (step 1). Limits were defined by the minimum and maximum arc angle values in the dataset. The mean (x, y, z) coordinates of each bin were then calculated to approximate an averaged tract skeleton (step 2). To avoid aberrant morphologies, angles less than 135 degrees between contiguous mean tract coordinates were rejected, and the number of bins reduced until all angles satisfied this requirement (46). Spline interpolation of the final mean voxel coordinates using interparc (available for download at http://www.mathworks.com/matlabcentral/fileexchange/34874-interparc) was then performed to generate a smoothed tract skeleton (step 3).

Along Tract Statistics Algorithm (Stage 2): During the second stage (see steps 4 and 5 in Supplemental Fig. 4) equidistant cross-sectional tract segments (i.e. bins) are established and diffusion indices subsequently analyzed within each cross sectional bin. First, a number of equidistant points, as measured by arc-length, along the spline-interpolated tract skeleton were calculated, as well as the linear vectors forming the path between each point. For three continuous data points and their vectors $\overrightarrow{ab}$ and $\overrightarrow{bc}$, a cross sectional plane was calculated through the central data point, b, (x_0, y_0, z_0) using vector mathematics and the scalar equation of a plane (see equations one and two below). This process was repeated for each equidistant point along the smoothed optic tract skeleton, except for the first and last points; where the normal vector (i.e. the line perpendicular to the ideal

cross-sectional plane) was defined as the line connecting the first and last points to either the following or preceding point, respectively.

$$Equation\ 1.\ Defining\ the\ normal\ vector: \quad \frac{\overrightarrow{ab} + \overrightarrow{bc}}{\left|\overrightarrow{ab} + \overrightarrow{bc}\right|} = \hat{n} = (a, b, c)$$

$$Equation\ 2.\ Scalar\ equation\ of\ the\ plane: \quad d = ax_0 + by_0 + cz_0$$

Where b represents the origin (x_0, y_0, z_0); $\hat{n}$ represents the normal vector of the cross sectional plane, and d is the plane centered on the origin.

Diffusion tensor imaging data associated with each voxel were then analyzed within each bin (i.e. set of voxels located between adjacent cross-sectional planes). Those data points falling outside the cross-sectional plane on either end of the calculated tract skeleton were discarded from the final analysis to clip possible outliers. The LIBSVM (http://www.csie.ntu.edu.tw/~cjlin/libsvm/) toolbox was used for the Support Vector Regression analysis (Figure 6).

Detailed Methods on the calculation of retinotopic information content with fMRI

We defined retinotopic voxels using 1 post-surgery run, and then tested the other post-surgery run as well as the pre-surgery runs; this was jackknifed to use the other post-surgery run for voxel definition and the remaining post-surgical run for test (and the test results averaged). Thus, the analysis of the fMRI data completely separated voxel definition from voxel test, and thus avoids issues associated with biased voxel selection and double dipping (48). The test consisted of calculating the multi-voxel pattern similarity (using linear correlation) within the ROI when the wedge occupied the same quadrant across even and odd revolutions of the wedge. Thus the final fMRI values consisted of r-values describing the consistency of the multi-voxel pattern elicited by the stimulus at each quadrant: high r-values indicate consistency of response to a given quadrant across the even and odd stimulus rotations (i.e. high retinotopic information content), while low r-values indicate an inconsistent response to the stimuli (i.e. low retinotopic information content). See Supp. Figure S5 for a schematic of this analysis.

Supp. Figure S1

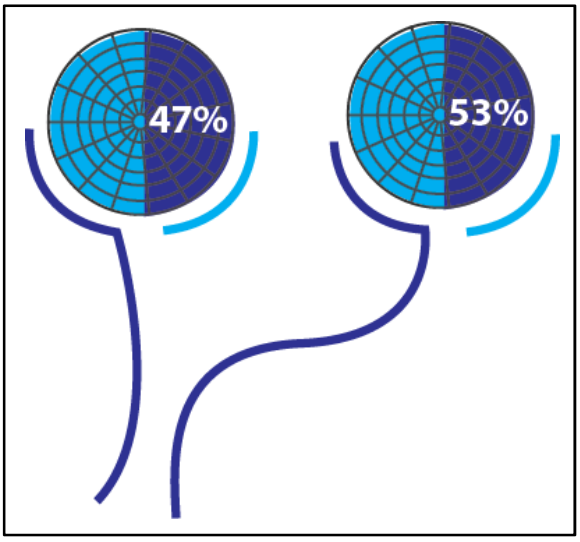

Supp. Figure S1. Schematic of weighting of visual performance data by optic tract. Representation of hemi-field specific visual field measurements (right hemi-field). Visual fields were analyzed with respect to visual hemi-field rather than eye, so that they could be compared with optic tract integrity fMRI retinotopy. Results were weighted using contributions of 47% temporal, and 53% nasal fibers (see ref 51).

Supp. Figure S2

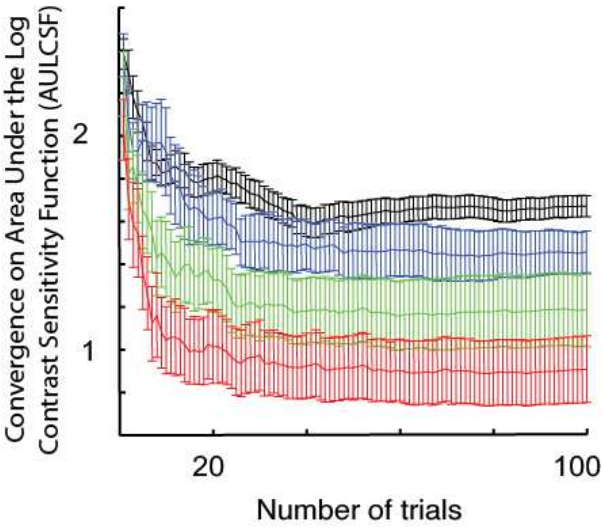

Supp. Figure S2. Convergence of AULCSF by trial number for all participants. The principal measure of contrast sensitivity, the area under the log contrast sensitivity function (AULCSF) is plotted by trial number (error bars over participants). As can be seen, AULCSF converges within 25 trials, and additional testing was carried out for each participant to increase precision of the test.

Supp. Figure S3

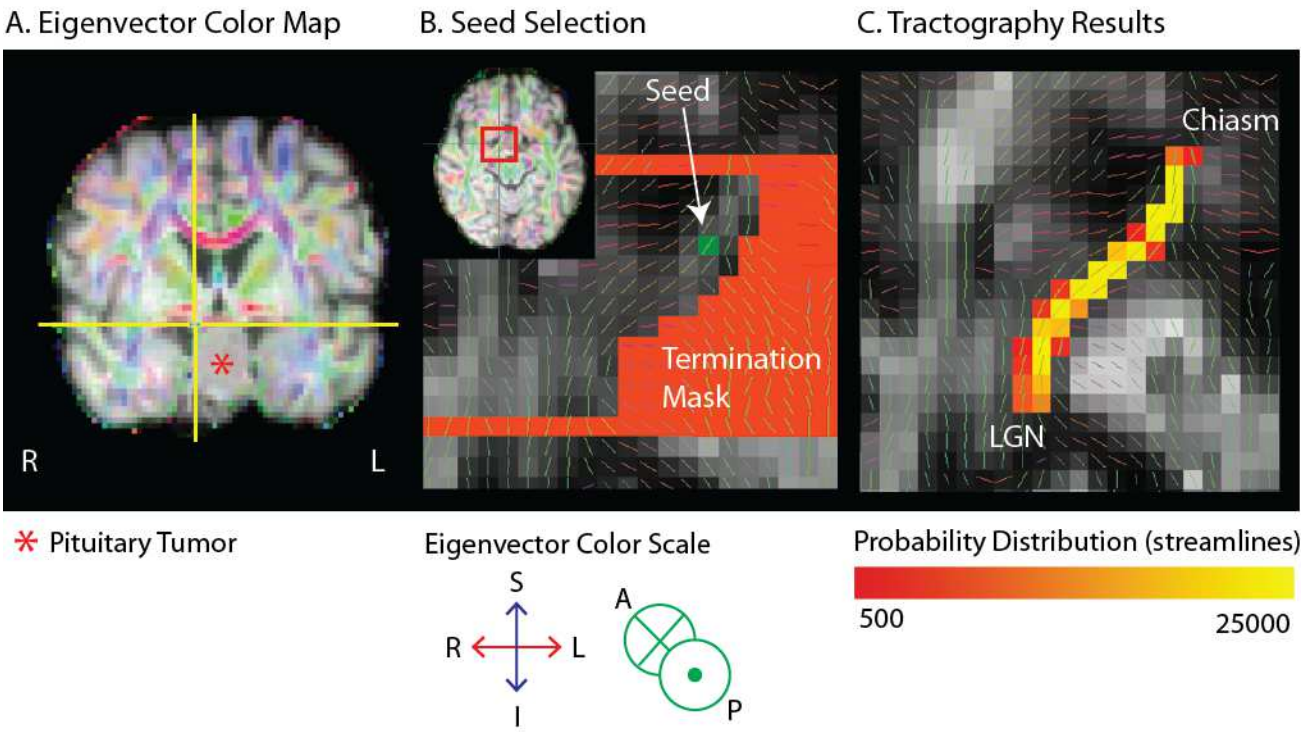

Supp. Figure S3. **Demonstration of tractography of the optic tract in a patient with a pituitary macroadenoma. (A).** The image shows a coronal T1-weighted MPRAGE MRI at the level of the pituitary gland transformed into diffusion space and overlaid on top of a principal eigenvector color map. The colors represent the direction of the principal eigenvector in each voxel (e.g. blue: superior-inferior orientation of fiber tracts; red: lateral-medial orientation; and green: anterior-posterior). The yellow crosshairs identify the right optic tract, which is compressed by a large pituitary tumor. **(B)** A magnified view of the MPRAGE image through a single axial slice at the level of the optic tract is displayed in the middle panel, with an arrow demarcating the probabilistic tractography seed mask. Approximately 25,000 streamlines, in all directions are sampled from the seed mask, generating a probability map that describes the likelihood of a connection between the seed and all other voxels in the brain. Probability is roughly defined as the number of streamlines that reach a particular voxel, using the principal eigenvector color map as a guide. In order to restrict tractography results to voxels located between the optic chiasm and lateral geniculate nucleus, streamlines were terminated when they entered the termination mask. **(C)** The results of our probabilistic tractography approach are displayed on the right, thresholded to include only those voxels in which greater than 2% of all streamlines from the seed mask passed through. The threshold was determined through visual inspection of the tractography results as the optimal value, which both removed outlying data points and preserved well-delineated optic tracts. It is also important to note that our thresholded tractography results are consistent with dimensions previously reported in post-mortem brains (43).

Supp. Figure S4

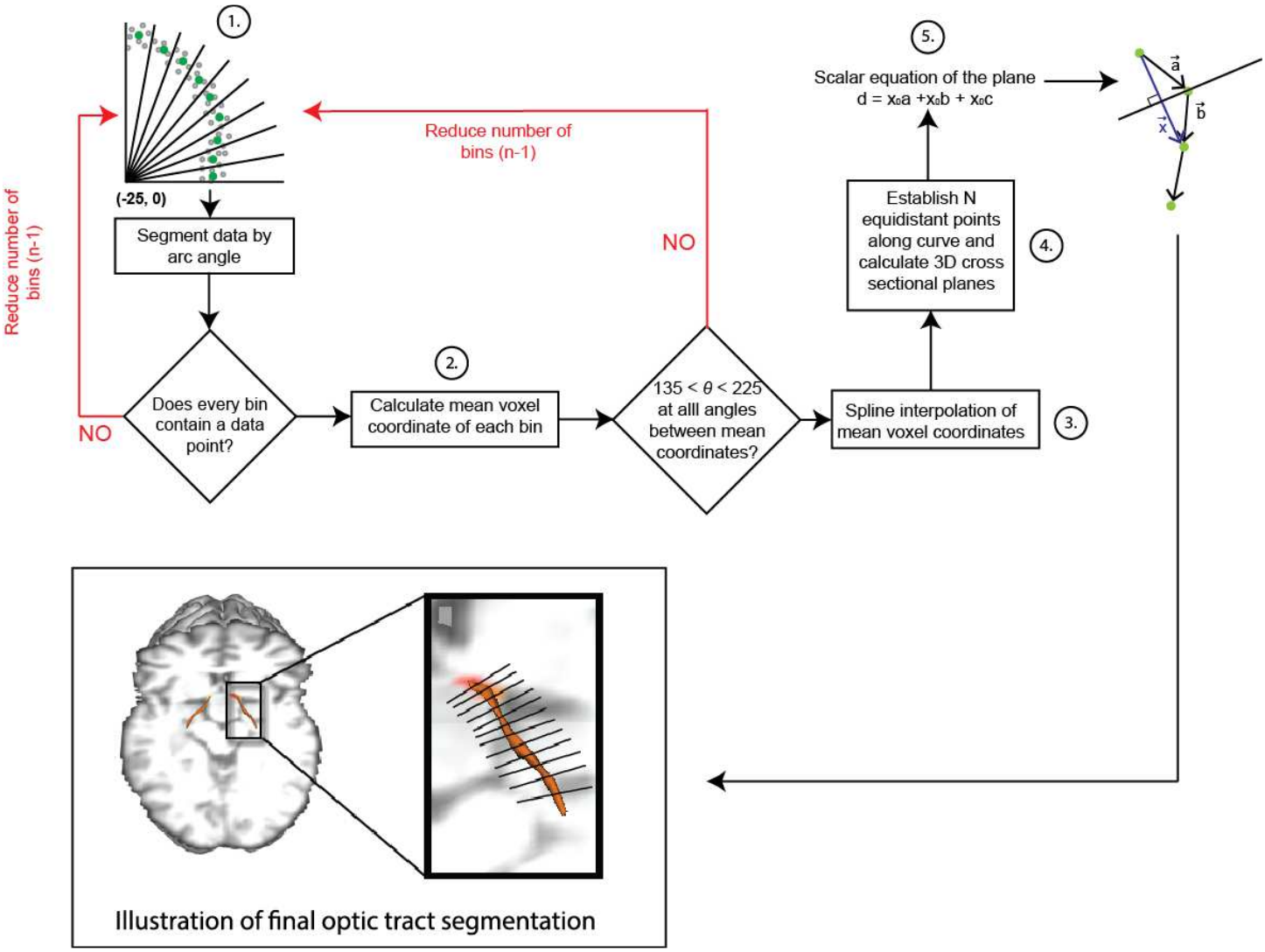

Supp. Figure S4. Schematic of along-tract statistics algorithm. Description of Along-tract Statistics Analysis Pipeline, adapted from the geospatial representation of river channels (50). Depicted is a flowchart outlining the steps required to segment the optic tract into equidistant cross-sectional bins. Also shown is an illustration of the final optic tract segmentation in a single compressive pituitary tumor subject. Note: the illustration is for descriptive purposes only. Adapted from Merwade et al., 2005.

Supp. Figure S5

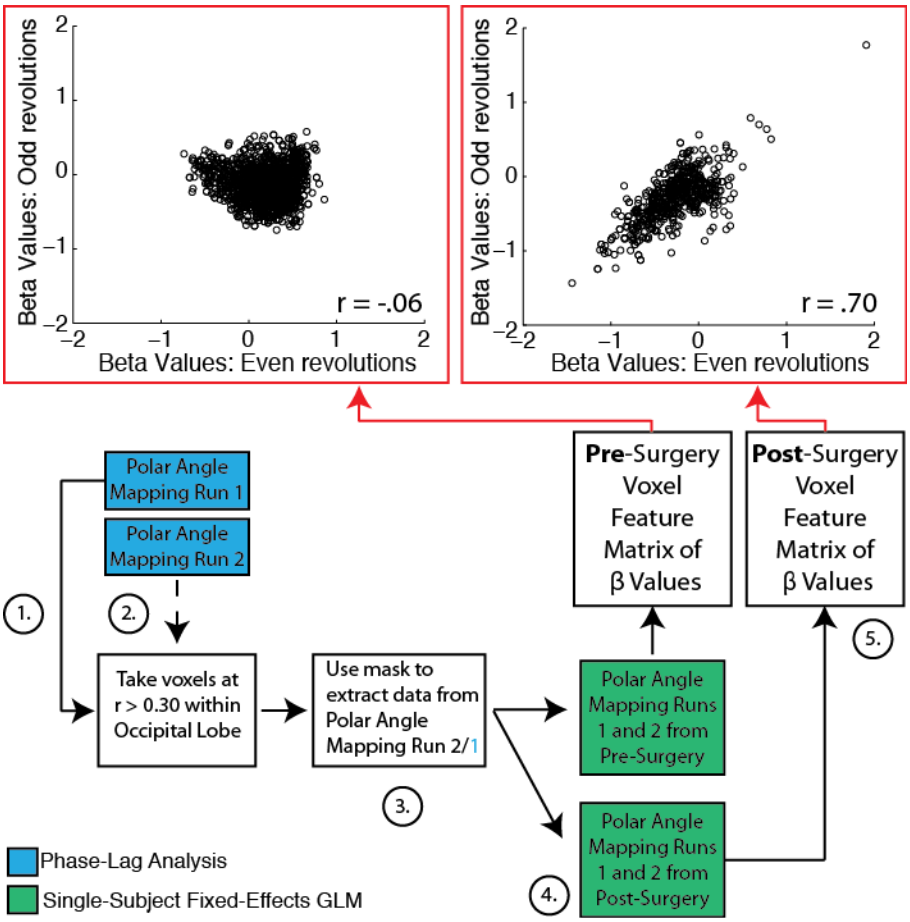

Supp. Figure S5. Schematic of multivoxel linear correlation analysis (MVPA). Depicted here is a flowchart describing the multivoxel linear correlation analysis, which shows r correlations in a single subject both before and after surgery. Refer to the main text and 'Materials and Methods' for a detailed description of each step. Critically, this measure of the fidelity of retinotopic activity is agnostic about whether there is reorganization of retinotopic maps when comparing pre- and post-surgical data: if the stimulus elicits a consistent pattern of activation across striate cortex voxels in even and odd revolutions, the fidelity of retinotopic information is high, and the r value is correspondingly high.

Supp. Figure S6

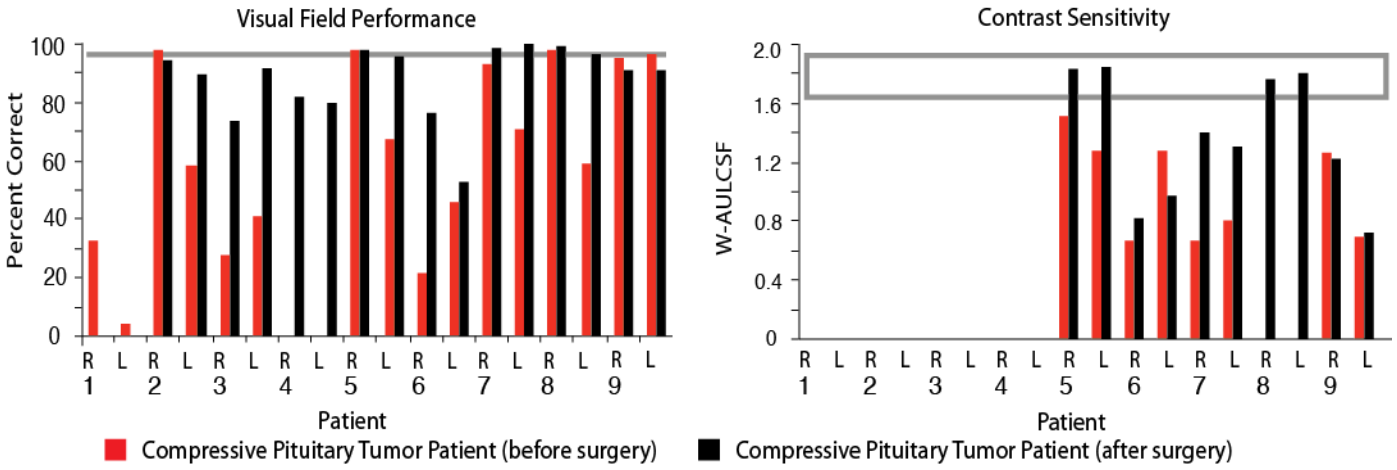

Supp. Fig. S6. Pre- and postoperative visual ability of each compressive pituitary tumor patient. Shown are the raw visual psychophysics data, before and after surgery, for all compressive pituitary tumor patients enrolled in our study. The gray boxes represent either the mean visual field acuity performance or AULCSF (area under the log contrast sensitivity function) across healthy control participants, with the upper bar representing one standard deviation above the mean, and the lower bar, one standard deviation below the control mean.

Supp. Figure S7.

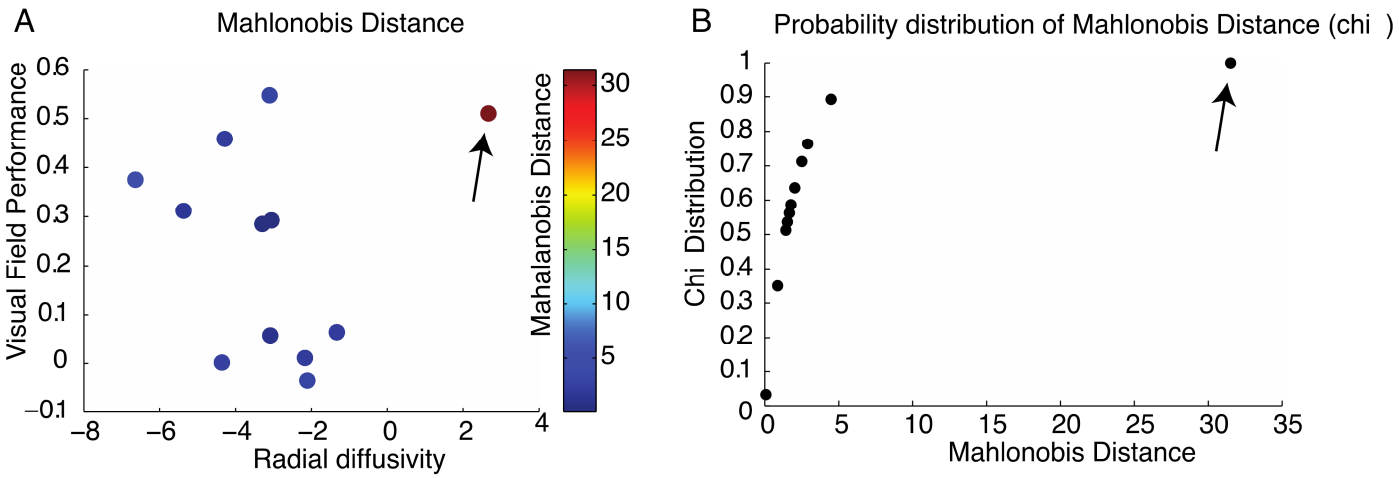

Supp. Figure S7. Identification of data outlier using Mahlonobis distance. Measurement of post-operative radial diffusivity (right optic tract) in a single subject, C1, did not follow the consistent pattern of reductions typically observed after surgical decompression in our cohort of subjects. Further analysis of this data point in the context of our complete data-set was warranted to determine if this represented an actual effect, possibly indicative of worse post-surgical visual outcomes, an artifact of DTI acquisition, or an artifact of unknown origin. **(A)** Using improvement in visual ability as the dependent variable (post-operative visual field performance minus pre-operative performance) and radial diffusivity improvement (post- minus pre-operative; measured as a tract averaged difference of a modified t-score) as the independent variable, we employed an iterative process to measure the Mahlonobis distance of each data point from the joint distribution of all other data points. The Mahlonobis distance, as opposed to Euclidean distance, takes into account the shape of the distribution (e.g. a data point located in the center of an ellipsoid-shaped distribution might naturally have a larger distance from the average than data points on either end). The data point for subject C1 (red) is furthest from the distribution. **(B)** To determine if this represented a statistically significant outlier rather than a data point on the tail of the distribution, a chi-squared distribution of the multivariate distance for each radial diffusivity and visual field improvement score revealed that radial diffusivity measured in the right optic tract of subject C1 (top right data point in Supp. Fig 7B) was significantly outside the likely distribution of our complete data-set ($p < 0.001$, $df = 2$). For these reasons, the hemisphere identified as an outlier in this analysis was excluded from the calculation of the relationship between the changes in DTI indices with the change in visual abilities (see Fig 4D in the main text).

Supp. Table S1. Demographic information of enrolled participants and tract averaged diffusion indices.

Compressive Pituitary Tumor Patients					FA (Right)		FA (Left)		MD (Right)		MD (Left)		AD (Right)		AD (Left)		RD (Right)		RD (Left)	
	Age	Sex	Description	Size (cm)*	Pre	Post	Pre	Post	Pre	Post	Pre	Post	Pre	Post	Pre	Post	Pre	Post	Pre	Post
C1	72	M	Macroadenoma	2.4 x 4.3 x 2.7	0.2478	0.2492	0.2835	0.3429	1.4026	1.5728	1.4138	1.2100	1.7816	1.9774	1.8543	1.6678	1.2132	1.3705*	1.1936	0.9811
C2	62	M	Macroadenoma	2.2 x 4.1 x 2.6	0.2450	0.2859	0.2850	0.3185	1.4696	1.1400	1.3903	1.2877	1.8432	1.5164	1.8299	1.7497	1.2828	0.9518	1.1705	1.0567
C3	53	F	Macroadenoma	3.0 x 4.8 x 2.1	0.2020	--	0.2824	--	1.5355	--	1.4032	--	1.8368	--	1.8262	--	1.3849	--	1.1916	--
C4	55	M	Macroadenoma	3.1 x 3.1 x 2.2	0.2887	0.3366	0.2294	0.2728	1.5432	1.3982	1.5974	1.3883	1.9923	1.8906	2.0047	1.8032	1.3186	1.1519	1.3937	1.1809
C5	65	M	Macroadenoma	2.1 x 3.2 x 2.4	0.1872	0.2902	0.2923	0.3463	1.8519	1.5176	1.3214	1.1934	2.2419	2.0072	1.7596	1.6560	1.6569	1.2728	1.1023	0.9620
C6	78	F	Macroadenoma	2.4 x 2.1 x 1.4	0.1793	0.2553	0.1775	0.2875	2.1186	1.5643	2.1809	1.8069	2.5437	2.0106	2.6099	2.3726	1.9061	1.3412	1.9664	1.5241
C7	53	M	Macroadenoma	2.2 x 2.9 x 2.1	0.1647	0.2467	0.3414	0.3737	1.5037	1.3391	1.2105	0.9068	1.7318	1.7147	1.6632	1.3026	1.3896	1.1513	0.9842	0.7089
C8	60	M	Macroadenoma	2.1 x 3.1 x 2.3	0.1942	0.2394	0.2015	0.2638	1.5844	1.5678	1.5844	1.3854	1.8890	1.9507	1.9193	1.7793	1.4321	1.3763	1.4170	1.1885
C9	64	M	Macroadenoma	3.4 x 2.8 x 2.0	--	0.1734	--	0.1813	--	1.5732	--	1.6552	--	1.8444	--	1.9469	--	1.4377	--	1.5094
Average	**62.4444**	**7M**			**0.2136**	**0.2596**	**0.2616**	**0.2983**	**1.6262**	**1.4591**	**1.5128**	**1.3542**	**1.9825**	**1.8640**	**1.9334**	**1.7848**	**1.4480**	**1.0772**	**1.3024**	**1.1389**
Std	**8.53099**				**0.0424**	**0.0473**	**0.0541**	**0.0610**	**0.2390**	**0.1568**	**0.2984**	**0.2800**	**0.2764**	**0.1718**	**0.2914**	**0.3015**	**0.2269**	**0.4579**	**0.3036**	**0.2771**
Non-compressive Pituitary Tumor Patients																				
NC1	36	F	Rathke's Cyst	1.2 x 0.8 x 0.7	0.3833	--	0.3838	--	1.0590	--	1.2096	--	1.5269	--	1.7323	--	0.8251	--	0.9482	--
NC2	56	F	Microadenoma	1.2 x 0.6 x 1.2	0.2845	--	0.3234	--	1.1894	--	1.0692	--	1.5645	--	1.4662	--	1.0018	--	0.8707	--
NC3	30	F	Macroadenoma	1.4 x 1.1 x 1.6	0.3338	--	0.3451	--	1.1281	--	1.1952	--	1.5449	--	1.6508	--	0.9197	--	0.9675	--
NC4	44	M	Microadenoma	1.1 x 1.2 x 0.7	0.2536	--	0.3346	--	1.5041	--	1.2808	--	1.9113	--	1.7527	--	1.3005	--	1.0449	--
NC5	39	M	GH Secreting	1.5 x 1.5 x 2.0	0.4151	--	0.3906	--	1.2063	--	1.2635	--	1.7746	--	1.8196	--	0.9221	--	0.9855	--
Average	**41**	**2M**			**0.3341**		**0.3555**		**1.2174**		**1.2037**		**1.6645**		**1.6843**		**0.9938**		**0.9634**	
Std	**8.76356**				**0.0599**		**0.0269**		**0.1524**		**0.0745**		**0.1525**		**0.1216**		**0.1632**		**0.0565**	
Healthy Control Participants																				
H1	58	F	--	--	0.4728	--	0.3662	--	1.1049	--	1.5022	--	1.7187	--	2.1054	--	0.7980	--	1.2006	--
H2	37	F	--	--	0.3869	--	0.3024	--	1.1516	--	1.5078	--	1.6728	--	2.0002	--	0.8910	--	1.2617	--
H3	44	M	--	--	0.3182	--	0.3372	--	1.2025	--	1.4057	--	1.6440	--	1.9413	--	0.9817	--	1.1379	--
H4	69	F	--	--	0.3809	--	0.4072	--	1.3704	--	1.2441	--	1.9210	--	1.8192	--	1.0951	--	0.9565	--
H5	45	M	--	--	0.3273	--	0.3345	--	1.1654	--	1.1926	--	1.5748	--	1.6365	--	0.9606	--	0.9707	--
H6	44	F	--	--	0.3831	--	0.3793	--	1.1188	--	1.1314	--	1.6238	--	1.6373	--	0.8664	--	0.8785	--
H7	41	F	--	--	0.2738	--	0.2887	--	1.5443	--	1.5603	--	1.9895	--	2.0502	--	1.3217	--	1.3154	--
H8	50	M	--	--	0.2510	--	0.3303	--	1.5451	--	1.0636	--	1.9737	--	1.4562	--	1.3308	--	0.8673	--
H9	45	F	--	--	--	--	--	--	--	--	--	--	--	--	--	--	--	--	--	--
Average	**48.1111**	**3M**			**0.3493**		**0.3432**		**1.2754**		**1.3260**		**1.7648**		**1.8308**		**1.0306**		**1.0736**	
Std	**9.77809**				**0.0713**		**0.0394**		**0.1853**		**0.1915**		**0.1689**		**0.2330**		**0.2024**		**0.1769**	

* Tumors were measured in the transverse, cranio-caudal, and antero-posterior dimensions.
** Refer to Supplemental Figure 2 for a detailed analysis of this data point.